

REDSHIFT EVOLUTION OF HIGHER-ORDER CORRELATIONS IN COSMIC LARGE-SCALE STRUCTURE WITH MINKOWSKI FUNCTIONALS

JAMES M. SULLIVAN,^{1,2} ALEXANDER WIEGAND,¹ AND DANIEL J. EISENSTEIN¹

¹*Harvard-Smithsonian Center for Astrophysics, 60 Garden St, Cambridge, MA, 02138, USA*

²*University of Texas at Austin, 110 Inner Campus Dr, Austin, TX 78705, USA*

ABSTRACT

We probe the higher-order galaxy clustering in the final data release (DR12) of the Sloan Digital Sky Survey Baryon Oscillation Spectroscopic Survey (BOSS) using germ-grain Minkowski Functionals (MFs). Our data selection contains 979,430 BOSS galaxies from both the northern and southern galactic caps over the redshift range $0.2 - 0.6$. We extract the higher-order part of the MFs and find deviations from the case without higher order MFs with χ^2 values of $\mathcal{O}(10^3)$ for 24 degrees of freedom across the entire data selection. We show the MFs to be sensitive to contributions up to the five-point correlation function across the entire data selection. We measure significant redshift evolution in the higher-order functionals for the first time, with a percentage growth between redshift bins of $15\% - 20\%$ in both galactic caps across all the functionals. This is nearly a factor of 2 greater than the growth in the two-point correlation term, and may have implications for the growth factor and the redshift evolution of the three-point and higher functions.

Keywords: methods: data analysis, methods: statistical, cosmology: observations, large-scale structure of Universe

1. INTRODUCTION

Cosmic large-scale structure is largely understood by characterizing and modeling observed galaxy distributions, which strongly influence the accepted cosmological model. Recent galaxy redshift surveys contain spectroscopic redshifts for of order $10^5 - 10^6$ galaxies, and their size makes them ideal testing grounds for exploring non-Gaussian features in this structure. Any quantitative analysis of such features must be firmly rooted in precise statistical measures. The most standardized of these measures is the spatial two-point correlation function ξ_2 (the probability of finding two galaxies within a certain distance), which is commonly used to constrain cosmological model parameters. However, observed structure is more complex than the purely Gaussian structure fully described by two-point statistics, and is in fact more intricate than the structure described by three-point statistics. Evidently, to accurately measure large-scale structure we must look to higher-order information in relation to these correlations.

The simplest approach is to calculate the correlation functions directly. While this has been widely achieved for the two-point function, and recently for the three-point function (Slepian & Eisenstein (2015) and Slepian et al. (2017)), fourth- and higher-order functions have yet to be well-determined. In fact, computing these functions directly is computationally infeasible (Wiegand & Eisenstein (2017)). There are various alternatives, and one of the most useful and rigorous is Minkowski Functional (MF) analysis. MFs quantitatively describe the geometry of extended bodies by mapping the shape of a body to real numbers. These functionals uniquely characterize the geometry and topology of a galaxy distribution, and contain information about all higher-order correlation functions.

MFs were first used to characterize large-scale structure by Mecke et al. (1994) in the form of the germ-grain model. This model pins down the morphology of the galaxy distribution by treating the survey galaxies as points (the germs) and decorating them with balls (the grains) whose scale-probing radius is the only model parameter. The union of these balls creates a set of extended bodies to which methods from integral geometry can be applied (For a review see Schmalzing (1999) or Schmalzing et al. (1996), and see Buchert (1995) for a short review.). We discuss this model further in the context of our analysis.

Another popular use of MFs lies in applying them to the isodensity contours of density fields, including galaxy and cluster surveys (e.g. Schmalzing et al. (1996), Kerscher et al. (1997), Kerscher et al. (1998), Kerscher et al. (2001a), and Kerscher et al. (2001b)), dark matter overdensity fields (Platzöder & Buchert (1996), Schmalzing & Buchert (1997), Sahni et al. (1998), Sathyaprakash et al. (1998), Schmalzing et al. (1999), Hikage et al. (2003), Nakagami et al. (2004),

Choi et al. (2013), and Blake et al. (2014)), and other astrophysical settings (Petri et al. (2013), Gleser et al. (2006), Einasto et al. (2014), and Yoshiura et al. (2017)). Still further work with MFs has recently used the isothermality contour maps of the CMB to constrain its Gaussianity (Ducout et al. (2013), Planck Collaboration et al. (2014a), and Planck Collaboration et al. (2014b), Planck Collaboration et al. (2016)). Clearly MFs are a powerful and widely-used tool in subfields across cosmological disciplines.

Here we focus on the germ-grain model, because recent work using the 7th and 12th data releases of SDSS-III (DR7 and DR12) of the Baryon Oscillation Spectroscopic Survey (BOSS) (Dawson et al. (2013)) has shown its use in accessing correlation information that cannot be calculated directly (DR7 paper - (Wiegand et al. (2014)) & DR12 paper - (Wiegand & Eisenstein (2017))), SDSS-III - Eisenstein et al. (2011)). We use the largest complete spectroscopic redshift survey to date, the complete DR12 dataset, to access unprecedented accuracy in the higher-order correlation functions. We also explore the redshift evolution of the higher-order correlations, which are expected to grow nonlinearly in time with varying behavior for different orders.

This paper is organized in a non-standard way. We try to guide the reader through the uncommon quantities by introducing them at the place where we first use them on the data. In this way, there is a more immediate visualization of the mathematical expressions which hopefully promotes understanding. Therefore, we start in Section 2 by describing our usage of the BOSS dataset. Section 3 and Section 4 then guide through the germ-grain model, its application to the data and our transformations of the MFs. Section 5 describes higher-order correlations and relates our analysis of redshift evolution. Section 6 presents our conclusions.

2. BOSS DATA

Our sample was collected with the 2.5m Sloan Telescope (Gunn et al. (2006)). For specifics on photometry and instruments, refer to Gunn et al. (1998), Fukugita et al. (1996), Lupton et al. (2001), Smith et al. (2002), Pier et al. (2003), Padmanabhan et al. (2008), Doi et al. (2010), as well as the eighth data release (Eisenstein et al. (2011)). For details on spectroscopic redshift determination see Smee et al. (2013) and Bolton et al. (2012). Our samples are drawn from the third phase of the SDSS (York et al. (2000)) Luminous Red Galaxy (LRG) catalog (Eisenstein et al. (2001)) of the BOSS (Dawson et al. (2016)) in DR12 (Alam et al. (2015)). For specifics regarding the data, see Reid et al. (2016).

2.1. Redshift Samples - CMASS and LOWZ

By using the full DR12 dataset, we access an unprecedented number of spectroscopic redshifts. We use the CMASS ("Constant (stellar) Mass") and LOWZ samples

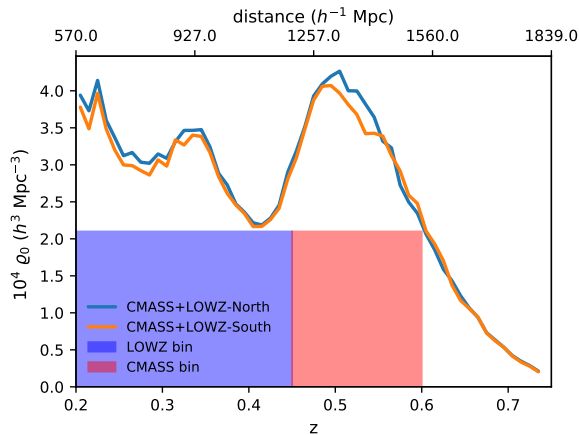


Figure 1. Minimum number density for the combined full CMASS, LOWZ, and LOWZE2 catalogs. By considering only values of ρ_0 that are at or below the minimum value over the combined sample, we need not restrict our analysis to differing densities at differing redshifts. The bins we call CMASS and LOWZ in this work are shown here.

(referring to low redshifts, or Low- z) samples, which are defined in detail by Reid et al. (2016). The CMASS sample was designed to expand upon the color cuts towards the blue in the SDSS-I and SDSS-II LRG samples, and has a redshift range of $0.45 \leq z \leq 0.75$. The LOWZ sample was designed to decrease the lower redshift bound of SDSS-I and SDSS-II down to $z = 0.2$, increasing the effective survey area by roughly a factor of 3. We consider two redshift bins (Fig. 1), which we will use CMASS ($0.45 \leq z \leq 0.60$) and LOWZ ($0.20 \leq z \leq 0.45$) to refer to from now on. The bins we use give a redshift range near triple that used in the DR12 paper. We use both the northern and the southern galactic caps (N- and SGC) of CMASS and LOWZ for an effective area of $9,376 \text{ deg}^2$. We also make use of the LOWZE2 sample (chunk 2 of the original LOWZ footprint), though it contributes a relatively small amount to the effective area and sample count (131 deg^2 , 2,985). There are a total of 979,430 galaxies in our two-bin sample, more than double the 410,615 used in the DR12 paper. The CMASS-South sample is approximately a factor of 2 smaller than its northern counterpart, and provides a much sparser coverage of the sky (Table 1). This has some effect on the behavior of the MFs, especially at large scales. LOWZ offers comparatively fewer observed galaxies, but has a better balance between the north and the south than CMASS does.

2.2. Survey and Corrections

We used a similar masking process to that of the DR12 paper. We considered only areas of the survey that were more than a distance of $2R$ from any inner or outer boundary of the data, where R is the common ball radius around each galaxy. This restricted our use of the data, more so for large values of R , but for MFs boundary corrections using random distri-

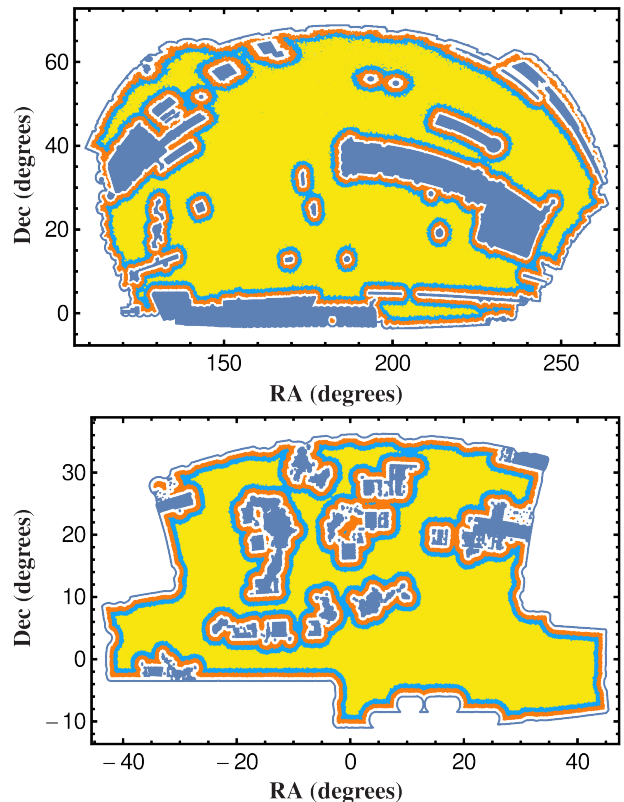


Figure 2. External and internal boundaries for the northern and southern patches analyzed. In blue the regions that we chose to define our boundary. In orange, light blue and yellow a projection of the regions 18, 36 and $54h^{-1}\text{Mpc}$ away from the nearest boundary. The boundary for the northern high- z bin is the same as in Wiegand et al. (2014).

butions are not effective. In correcting for bad and missing data, we used veto masks to remove galaxies based on effects such as poor spectral seeing, extinction, areas without observations and poor photometric conditions. The masks for both caps are provided in Fig. 2. The LOWZ sample especially has a comparatively large number of holes and covers a smaller area of the sky. We see the effects of this on our analysis, especially at low densities.

2.3. MD Patchy Mocks

We use mock data realizations to compare the correlations in the BOSS data to those of the cosmological concordance model. The mocks used in our analysis are from the MultiDark(MD)-Patchy mock galaxy catalogs (Kitauro et al. (2016)). These mocks were specifically produced to reflect the number density of the data, and were produced by referencing a large N-body simulation (BigMultiDark). We used the same ΛCDM cosmology as the simulation, which is the Planck1 cosmology, with $\Omega_M = 0.307115$, $\Omega_\Lambda = 0.692885$, $\Omega_b = 0.048$, $\sigma_8 = 0.8288$, and $h = 0.6777$. As indicated in the DR12, these mocks are very well suited for comparison when

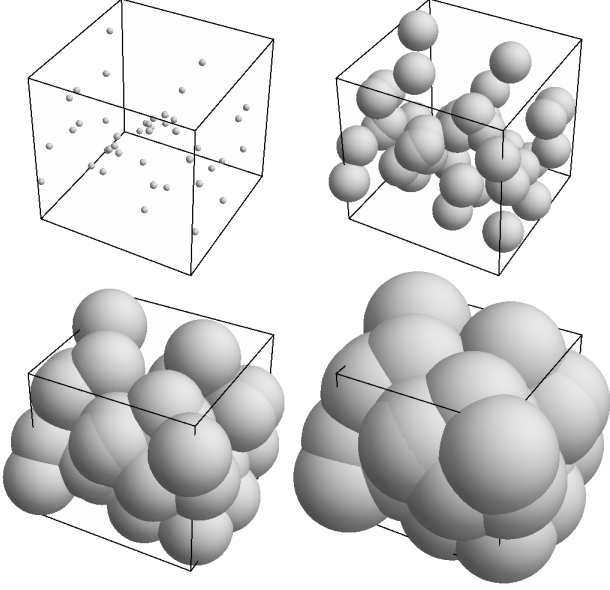


Figure 3. Illustration of the germ-grain procedure to transform a set of galaxies into an extended body. The galaxy positions are surrounded by balls of a common radius R . Then the MFs of the body formed by the union of all the balls are studied as a function of R . From Wiegand et al. (2014).

calculating the higher-order parts of the MFs, although there is light tension between the data and the MD-Patchy power spectrum that may be relieved by a 5% reduction in the mock power spectrum amplitude. We used 997 mock survey realizations for CMASS-North (the same as for the DR12 paper), 399 mocks for CMASS-South and LOWZ-North, and 383 mocks for LOWZ-South in our calculations using the CHIPMINK code. These large numbers of mock realizations allow us to derive correlation-conscious uncertainties when comparing the data to the concordance model.

Table 1. Reduced set of basic parameters of the SDSS DR12 CMASS and LOWZ samples.

| Sample | CMASS | | | LOWZ | | |
|------------------------------------|---------|---------|---------|---------|---------|---------|
| | NGC | SGC | total | NGC | SGC | total |
| N_{gal} | 607,357 | 228,990 | 836,347 | 177,336 | 132,191 | 309,527 |
| Effective area (deg ²) | 6,851 | 2,525 | 9,376 | 5,836 | 2,501 | 8,337 |
| $N_{\text{gal}}(\text{our bins})$ | 410,617 | 294,091 | 704,708 | 151,003 | 123,719 | 274,722 |

3. THE GERM-GRAIN MODEL

In this Section, we provide an abbreviated description of Minkowski Functionals. For a more complete explanation of the germ-grain model, see the DR7 paper.

3.1. Minkowski Functionals

We apply a result from integral geometry (Hadwiger 1957) to express the MFs as a linear combination of 4 base functionals in three-dimensional Euclidean space. We choose a normalization of the base functionals (denoted $V_0 - V_3$) that correspond to familiar geometric quantities as follows:

$$V_0 = V ; V_1 = \frac{S}{6} ; V_2 = \frac{H}{3\pi} ; V_3 = \chi . \quad (1)$$

Here V is the volume of the extended body, S is its surface area, H is the integral mean curvature of the surface, and χ is the topological Euler characteristic or integral Gaussian curvature. To refresh the reader, H is the average of the curvature of a surface over all angles and χ is the sum of independent components and cavities minus the number of holes.

The germ-grain model connects MFs and observed galaxy distributions. The germ-grain procedure is to take a point distribution of "germs" and surround each point with a convex body, or "grain." By taking a galaxy distribution with positions $\{\mathbf{x}_1, \dots, \mathbf{x}_N\}$ as the point distribution, and using balls (filled spheres) of radius R as the convex body, we create an extended body from the union of the spheres. The MFs can now be used to describe the relatively simple extended body that is transformed from the observed galaxy distribution (Fig. 3).

The MFs clearly depend on the common ball scaling radius R , but they also depend on the sample density ϱ_0 of the observed distribution due to the germ-grain construction. The radius R is a tunable parameter that we alter in our analysis to probe different scales of structure. When exploring the density parameter space, we randomly sample from either the mock or data distribution at different values of ϱ_0 . These values are determined by downsampling at fixed percentages from the height of our bins. At low densities, this tends to erase structure and the MF's approach Poissonity.

4. MEASURING MFS

In this Section, we describe the quantities we measure for each sample.

4.1. Functional Densities

To measure the MFs for our samples, we must calculate the MFs of the individual balls. These *partial MFs* are then taken as an ensemble of statistical quantities. Rather than work with the extrinsic quantities V_μ , we use the survey volume V_{Survey} to define the intrinsic functional densities v_μ :

$$v_\mu \equiv V_\mu / V_{\text{Survey}} ; \mu \in \{0, \dots, 3\} \quad (2)$$

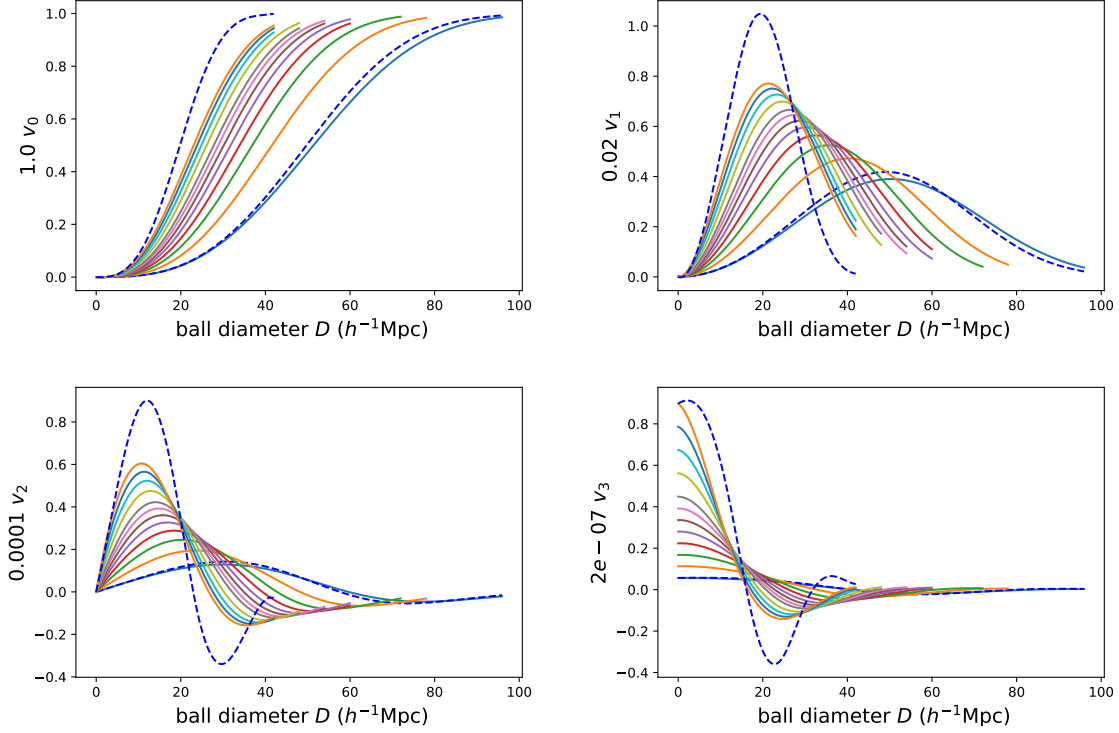


Figure 4. MF densities v_μ for the CMASS-North MD-Patchy mock files within a sample density range of 5% to 80% of the reference density $\varrho_0 = 2.08 \times 10^{-4} h^3 \text{Mpc}^{-3}$. The most extreme densities are plotted along with their theoretical Poisson point distributions (blue dotted lines). At the lowest density the MFs approach the Poisson curves, and at the highest density show the greatest difference from the Poisson curves.

The analytic expressions for these v_μ are given by:

$$\begin{aligned} \langle v_0 \rangle &= 1 - e^{-\varrho_0 \bar{V}_0}, \\ \langle v_1 \rangle &= \varrho_0 \bar{V}_1 e^{-\varrho_0 \bar{V}_0}, \\ \langle v_2 \rangle &= \left(\varrho_0 \bar{V}_2 - \frac{3\pi}{8} \varrho_0^2 \bar{V}_1^2 \right) e^{-\varrho_0 \bar{V}_0}, \\ \langle v_3 \rangle &= \left(\varrho_0 \bar{V}_3 - \frac{9}{2} \varrho_0^2 \bar{V}_1 \bar{V}_2 + \frac{9\pi}{16} \varrho_0^3 \bar{V}_1^3 \right) e^{-\varrho_0 \bar{V}_0}, \end{aligned} \quad (3)$$

where $\langle v_\mu \rangle$ refer to the average functional densities over the distribution, and \bar{V}_μ refer to the unnormalized modified MFs (Wiegand et al. (2014)). The v_μ as measured for the mocks are shown in Fig. 4. Their behavior as a function of R (or diameter D in this case) and ϱ_0 is intuitive: as R increases the volume of the survey box occupied by the balls is saturated as v_0 approaches unity, and an decrease in density delays this saturation. The other functionals are slightly less transparent, but show that there is some maximum in the uncovered surface area when R is increased, and a similar maximum and minimum in curvature and Euler characteristic. For the surface area, a decrease in density will delay the maximum as a function of radius, and for the remaining two MF densities, the density affects the amplitude of the functional.

4.2. Transforming the Densities

Observed galaxy distributions have significant structure, and thus must employ the full form of \bar{V}_μ in Eq. (3). But for the case of a Poisson distribution, the unnormalized modified MFs \bar{V}_μ are given for a ball B by the familiar quantities:

$$\begin{aligned} V_0(B) &= \frac{4\pi}{3} R^3; \quad V_1(B) = \frac{2}{3} \pi R^2; \\ V_2(B) &= \frac{4}{3} R; \quad V_3(B) = 1. \end{aligned} \quad (4)$$

These are intuitive and convenient to work with, and we use the Poisson case as a reference in analyzing distributions with more structure. Following from this choice, we adopt the dimensionless transformed MFs η_μ :

$$\eta_\mu \equiv \bar{V}_\mu / V_\mu(B). \quad (5)$$

The mapping from v_μ to η_μ retains the information about the MFs as a function of R and ϱ_0 , but the latter provides a better perspective in terms of the higher-order correlations. To see this, we can rewrite the dimensionless MFs as the following power series:

$$\eta_\mu = \sum_{n=0}^{\infty} \frac{c_{\mu,n+1}}{(n+1)!} (-\varrho_0 V_0(B))^n \quad (6)$$

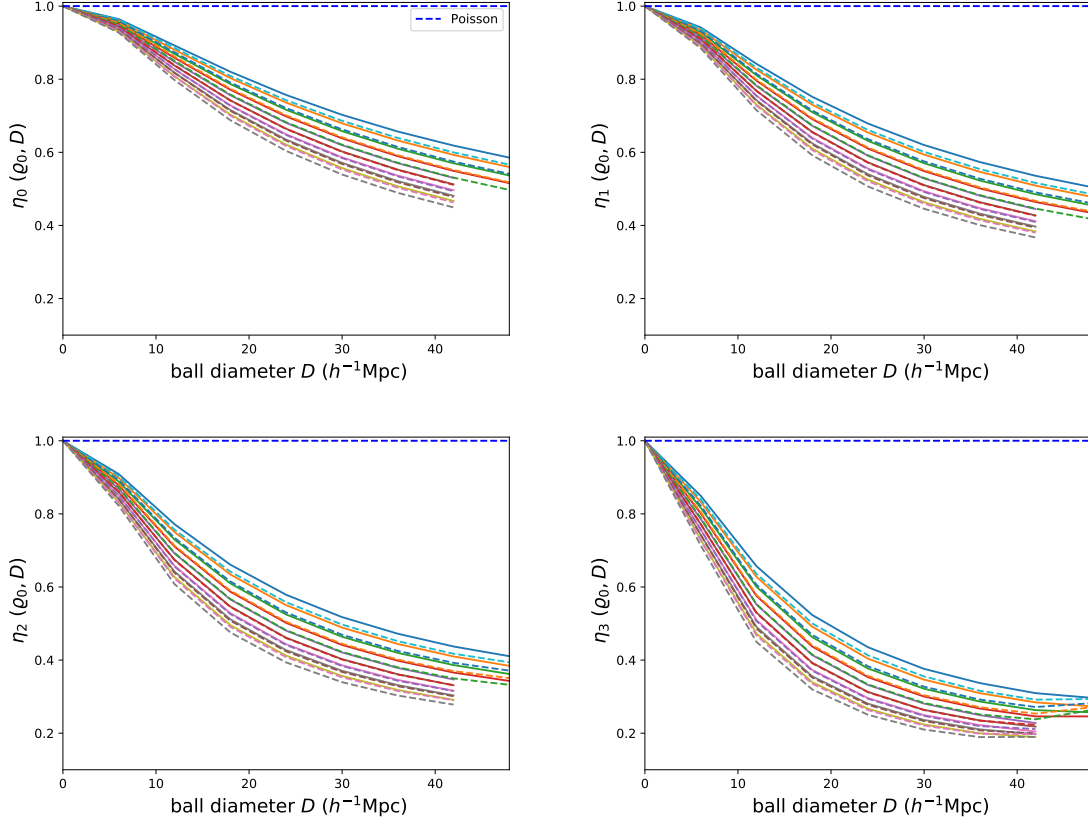


Figure 5. Dimensionless transformed MFs in the Southern Galactic Cap for evaluated for 399 SDSS DR12 MD-Patchy mocks plotted as a function of ball diameter. CMASS-South values are solid, LOWZ-South values are dashed. These quantities can be more directly related to the correlation functions than the v_μ can. The difference in the functionals between the redshift bins is visible across all the MFs.

where $c_{\mu,1} = 1$ and

$$c_{\mu,n+1}(R) = V_0^{-n}(B) \int \xi_{n+1}(0, \mathbf{x}_1, \dots, \mathbf{x}_n) \times \frac{V_\mu(B \cap B_{\mathbf{x}_1} \cap \dots \cap B_{\mathbf{x}_n})}{V_\mu(B)} d^3x_1 \dots d^3x_n \quad (7)$$

where $V_\mu(B \cap B_{\mathbf{x}_1} \cap \dots \cap B_{\mathbf{x}_n})$ are the weighting functions).

Here, each term of the series is the integral of the product of the n -point correlation function ξ_{n+1} and a weighting function that depends on the balls (and therefore R). There is also a factor that includes the sample density ϱ dependence that may be considered independent of the correlation-dependent integral. Now we have a quantity conveniently defined on the unit interval $[0, 1]$ (for standard cosmological structure) that can be more easily compared in terms of our parameters. Fig. 5 shows the nine highest density samples (40% - 80% of $\varrho_0 = 2.08 \times 10^{-4} h^3 \text{ Mpc}^{-3}$) of η_μ as a function of D and now gives a measure of the non-Poisson behavior of the MFs. The MFs deviate further from Poisson behavior as D and ϱ_0 increase, approaching the structure of the full galaxy distribution, and illustrating the increased non-Poissonity at large

scales. Visually the MFs are on the order of 1% different between the redshift bins, so already the redshift evolution in the MFs is evident. However, we have yet to isolate higher-order contributions of the MFs, which we discuss in the next section.

5. HIGHER-ORDER CONTRIBUTIONS TO THE MFs

This Section describes our analysis of the isolated higher-order contributions to the MFs. In the interest of conserving page space, we will often choose η_1 as a proxy for the behavior of all the MFs, which is similar to that of η_1 .

5.1. The Two-point Function

To measure higher-order correlations, we subtract the two-point correlation function contribution to the MFs. To do this, we must first calculate the two-point term. Ignoring the higher-order terms ($n \geq 3$) of Eqn. (6) we are left with:

$$\eta_\mu = 1 - \frac{\varrho_0}{2} \int d^3x_1 \xi_2(0, \mathbf{x}_1) \frac{V_\mu(B \cap B_{\mathbf{x}_1})}{V_\mu(B)}. \quad (8)$$

We assume isotropic correlations, and upon transforming to spherical coordinates (8) becomes:

$$\eta_\mu = 1 - 2\pi\varrho_0 \int_0^{2R} \frac{V_\mu(R, r)}{V_\mu(B(R))} \xi_2(r) r^2 dr. \quad (9)$$

where the integral is zero if the centers of the balls are more than $2R$ apart. This is the same as Eqn. (6) for $n = 1$ barring the factor of $V_0(B)$.

We can write the weight functions $V_\mu(B \cap B_1)$ as:

$$V_0(r) = \frac{1}{12} \pi (2R - r)^2 (r + 4R); \quad (10)$$

$$V_1(r) = \frac{1}{3} \pi R (2R - r); \quad (11)$$

$$V_2(r) = \frac{2}{3} (2R - r) + \frac{2}{3} R \sqrt{1 - \left(\frac{r}{2R}\right)^2} \arcsin\left(\frac{r}{2R}\right); \quad (12)$$

$$V_3(r) = 1, \quad (13)$$

where R is again the radius of the balls and r is the integration variable. The weights then conveniently define integration windows for ξ_2 for the different functionals, and as μ increases, so does the R at which the structure is probed.

Using independently determined values of ξ_2 , we compare the two-point coefficient of Eqn. (8) to the mathematically equivalent integrated two-point function Eqn. (9). The integrated two-point correlation functions match up fairly well to the $c_{\mu,2}$ coefficients at all but the highest scales we probed. It is reassuring to find this match in both redshift bins and in both galactic caps, because the MD-Patchy mocks were designed to match the two-point correlation function. We detect redshift evolution between the CMASS and LOWZ is detected in the two-point function, with growth between bins of approximately 10%.

5.2. Higher-order Functionals

We isolate only the higher-order contributions to the MFs to determine their effect on the higher order correlations. Subtracting the two-point contribution Eqn. (9) from the power series expression for η_μ , we take only the terms with $n \geq 2$ in Eqn. (6) as the higher-order part of the functionals, which we define as η_μ^h .

The higher-order functionals η_μ^h are a significant portion of the calculated functionals η_μ . Fig. 6 shows $\eta_\mu^h(D = 36 h^{-1} \text{ Mpc})$ for both redshift samples. We measure the significance of the detection by computing χ^2 values with 24 degrees of freedom for the mocks and the zero line and find values of order 10^3 , indicating a highly significant contribution of higher-order correlations to the structure of the distribution. In the limit of low sampling density, the higher-order part seems negligible, reflecting the near two-point structure characteristic of a completely Gaussian point distribution. Though it seem intuitive to expect this in the

Table 2. The χ^2 values of significance for the deviation from the zero line of the higher order functionals η_μ^h with 24 degrees of freedom at $D = 36 h^{-1} \text{ Mpc}$.

| μ | CMN | LZN | CMS | LZS |
|-------|------|------|-----|-----|
| 0 | 3447 | 2051 | 926 | 563 |
| 1 | 2871 | 1710 | 789 | 525 |
| 2 | 2011 | 1241 | 571 | 403 |
| 3 | 1057 | 700 | 317 | 251 |

Table 3. The χ^2 values of significance for the growth between the CMASS and LOWZ redshift bins for η_μ^h in each galactic cap at $D = 36 h^{-1} \text{ Mpc}$ for 24 degrees of freedom.

| μ | NGC | | SGC | |
|-------|----------|------------|----------|-----------------------|
| | χ^2 | σ_G | χ^2 | σ_G |
| 0 | 59.7 | 3.98 | 13.4 | 5.18×10^{-2} |
| 1 | 36.0 | 1.92 | 7.19 | 4.56×10^{-4} |
| 2 | 25.2 | 0.85 | 5.81 | 6.66×10^{-5} |
| 3 | 14.9 | 0.09 | 3.63 | 6.34×10^{-7} |

Table 4. The χ^2 values of significance for the deviation between the NGC and SGC for η_μ^h in each redshift bin at $D = 36 h^{-1} \text{ Mpc}$ for 24 degrees of freedom.

| μ | NGC | | SGC | |
|-------|----------|-----------------------|----------|-----------------------|
| | χ^2 | σ_G | χ^2 | σ_G |
| 0 | 8.34 | 1.63×10^{-3} | 11.3 | 1.69×10^{-2} |
| 1 | 3.57 | 5.25×10^{-7} | 7.67 | 7.90×10^{-4} |
| 2 | 3.43 | 3.52×10^{-7} | 6.30 | 1.40×10^{-4} |
| 3 | 2.74 | 3.28×10^{-8} | 4.05 | 1.94×10^{-6} |

low-density limit, there is no theorem that would require a structured point process to pass through a stage of Gaussianity when the density is reduced. Regardless, the two-point behavior increasingly fails to describe the higher-order MFs as the sample density increases, meaning the integrated three and higher point functions must be non-zero, quantitatively capturing non-Gaussianity of the density field.

The data fit very well to the mocks, and nearly all the points lie within the $1 - \sigma$ error bars. We draw from this agreement the conclusion that the higher-order correlations are well described by the Planck1 concordance model, insofar as the MD simulation reflects it. Quantifying this, we find χ^2 values for 24 degrees of freedom of order 10 when comparing η_μ^h for the mocks and data. There is a known issue with η_0^h in the limit of low ϱ_0 where the values very slightly differ from zero, which should not occur by design. This is most

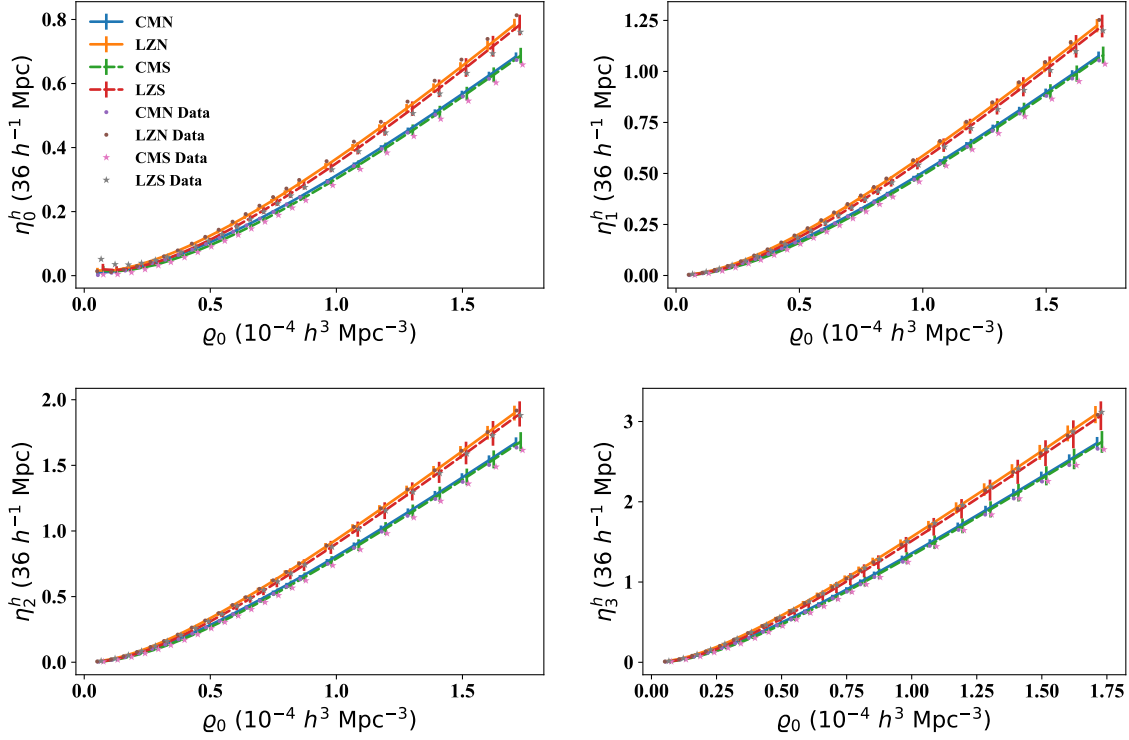


Figure 6. The higher-order contribution to the MFs η_{μ}^h as a function of density ρ_0 . The solid lines are the MD-Patchy mock values with 1σ error bars.

visible for LOWZ-South, and may be attributed to the mask construction.

The branching between the curves for the different redshift bins exhibits the redshift evolution in the structure, which grows at higher densities. However, a more targeted view of the redshift evolution shows that the percentage difference in η_{μ}^h is relatively constant as a function of density. Fig. 7 shows this percentage growth from the higher redshift CMASS bin to the lower redshift LOWZ bin. The percentage growth in fact decreases from near 25% as the density increases. Compared to the two-point percentage growth of $\approx 10\%$, this is a factor of two greater for the higher-order contribution to the MFs.

The percentage growth values for the NGC seem to agree with the mocks very well, and are close, if not within, the 1σ error bars. For the SGC the agreement is weaker, but seems to but strengthens as the density increases. Even if we were to take the trend of the SGC values literally they are generally greater than those of the NGC or the mocks, and would indicate a higher percentage growth if anything. However, we expect this deviating behavior to be a result of our treatment of the SGC.

6. SUMMARY & CONCLUSIONS

In this paper, we perform an unprecedented analysis of higher-order correlation information on the largest spectro-

scopic redshift survey to date. We use Minkowski Functional analysis along with independently calculated two-point correlation functions to measure non-Gaussianity in large-scale structure. Our detection of non-Gaussianity is highly significant, with χ^2 values of $\mathcal{O}(10^3)$ for 24 degrees of freedom across the NGC and SGC of the SDSS-III DR12.

We also measure the percentage growth in redshift of the higher-order part of MFs for the first time. This growth is measured to be 15%–20%, depending on density. We show the redshift evolution of non-Gaussianity is greater in the sum of the higher-order contributions to the MFs than in the two-point term by a factor of 2.

Our results motivate multiple avenues for future analysis of higher-order correlations, including measurement of the growth of the three-point and four-point functions. The growth in the higher-order correlations may also be applied in relation to the linear growth rate.

Acknowledgments

The SAO REU program is funded by the National Science Foundation REU and Department of Defense ASSURE programs under NSF Grant AST-1659473, and by the Smithsonian Institution. This research has also made use of results from NASA’s Astrophysics Data System.

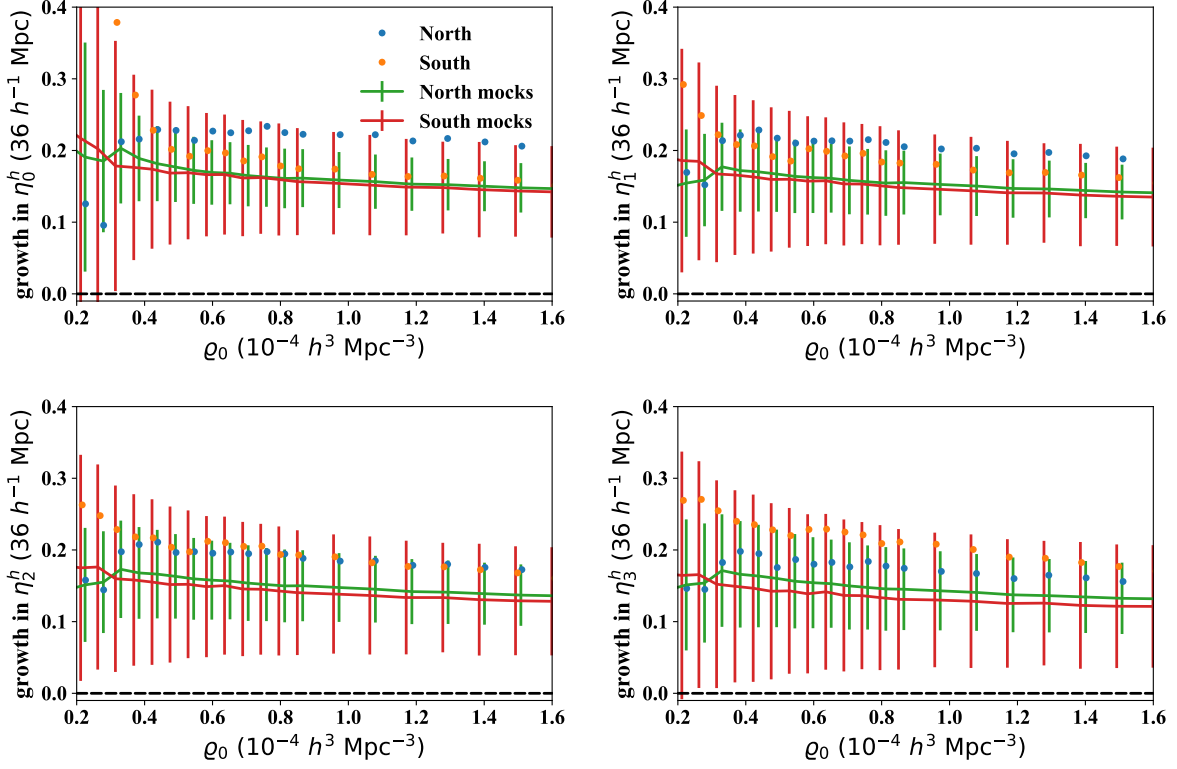


Figure 7. The percentage growth of the higher-order term of the functionals between redshift bins. Visually there is a 15%–20% growth from the higher redshift bin to the lower redshift bin. The MD-Patchy mocks are the solid lines with 1σ error bars, and the data are given by the points. The zero line is shown in black for comparison to the no-growth case.

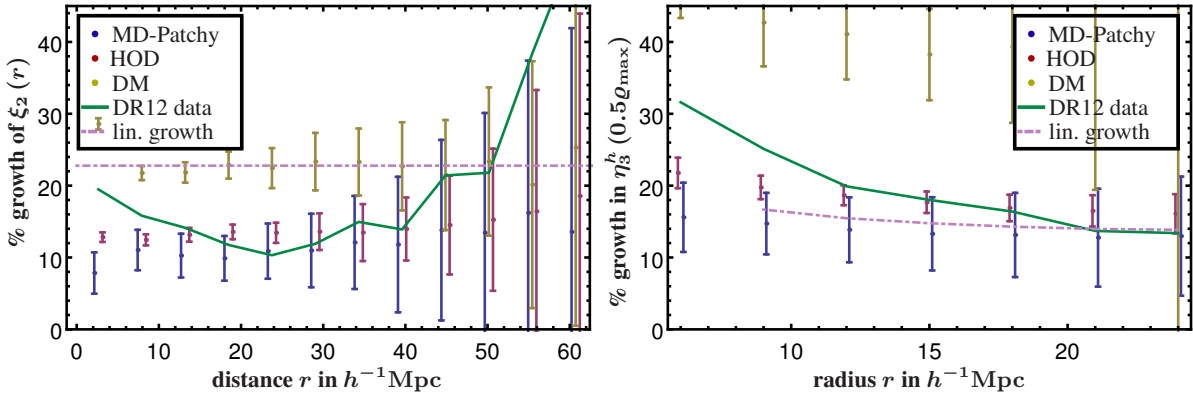


Figure 8. Comparison of the growth of two-point and higher order correlations between our two redshift bins for different cases. Blue points with error bars show the mean and 1σ contours derived from the MD-Patchy mocks. The red points show the same for the galaxy samples derived from our own HOD model, and the yellow points show the growth of the underlying dark matter field. The green solid line is the values for the galaxies from the final DR 12 sample. Their points have been joined by a line for better visibility, but measured values are for the same r . The dashed line in the two-point case indicates the linear growth expected for a Λ CDM model. In the η^h case it shows the expected growth when scaling all higher order-function by their corresponding powers of the growth factor (see text). Growth in η^h is at 50% of the maximal density, but as can be seen from Fig. 7, density dependence is very modest.

Funding for SDSS-III has been provided by the Alfred P. Sloan Foundation, the Participating Institutions, the National Science Foundation and the US Department of Energy Office of Science. The SDSS-III website is <http://www.sdss3.org/>.

SDSS-III is managed by the Astrophysical Research Consortium for the Participating Institutions of the SDSS-III Collaboration including the University of Arizona, the Brazilian Participation Group, Brookhaven National Laboratory, Carnegie Mellon University, University of Florida, the French Participation Group, the German Participation Group, Harvard University, the Instituto de Astrofísica de Canarias,

the Michigan State/Notre Dame/JINA Participation Group, Johns Hopkins University, Lawrence Berkeley National Laboratory, Max Planck Institute for Astrophysics, Max Planck Institute for Extraterrestrial Physics, New Mexico State University, New York University, Ohio State University, Pennsylvania State University, University of Portsmouth, Princeton University, the Spanish Participation Group, University of Tokyo, University of Utah, Vanderbilt University, University of Virginia, University of Washington and Yale University.

Software: CHIPMINK

REFERENCES

- Alam, S., Ho, S., Vargas-Magaña, M., & Schneider, D. P. 2015, [MNRAS](#), **453**, 1754
- Blake, C., James, J. B., & Poole, G. B. 2014, [MNRAS](#), **437**, 2488
- Bolton, A. S., Schlegel, D. J., Aubourg, É., et al. 2012, [AJ](#), **144**, 144
- Buchert, T. 1995, in *Large Scale Structure in the Universe*, ed. J. P. Mückel, S. Gottloeber, & V. Müller, 156
- Choi, Y.-Y., Kim, J., Rossi, G., Kim, S. S., & Lee, J.-E. 2013, [ApJS](#), **209**, 19
- Dawson, K. S., Schlegel, D. J., Ahn, C. P., et al. 2013, [AJ](#), **145**, 10
- Dawson, K. S., Kneib, J.-P., Percival, W. J., et al. 2016, [AJ](#), **151**, 44
- Doi, M., Tanaka, M., Fukugita, M., et al. 2010, [AJ](#), **139**, 1628
- Ducout, A., Bouchet, F. R., Colombi, S., Pogosyan, D., & Prunet, S. 2013, [MNRAS](#), **429**, 2104
- Einasto, M., Lietzen, H., Tempel, E., et al. 2014, [A&A](#), **562**, A87
- Eisenstein, D. J., Annis, J., Gunn, J. E., et al. 2001, [AJ](#), **122**, 2267
- Eisenstein, D. J., Weinberg, D. H., Agol, E., et al. 2011, [AJ](#), **142**, 72
- Fukugita, M., Ichikawa, T., Gunn, J. E., et al. 1996, [AJ](#), **111**, 1748
- Gleser, L., Nusser, A., Ciardi, B., & Desjacques, V. 2006, [MNRAS](#), **370**, 1329
- Gunn, J. E., Carr, M., Rockosi, C., et al. 1998, [AJ](#), **116**, 3040
- Gunn, J. E., Siegmund, W. A., Mannery, E. J., et al. 2006, [AJ](#), **131**, 2332
- Hadwiger, H. 1957, *Vorlesungen über Inhalt, Oberfläche und Isoperimetrie, Die Grundlehren der mathematischen Wissenschaften in Einzeldarstellungen mit besonderer Berücksichtigung der Anwendungsgebiete ; 93 (Springer)*, XIII, 312 S.: graph. Darst.
- Hikage, C., Schmalzing, J., Buchert, T., et al. 2003, [PASJ](#), **55**, 911
- Kerscher, M., Mecke, K., Schmalzing, J., et al. 2001a, [A&A](#), **373**, 1
- Kerscher, M., Schmalzing, J., Buchert, T., & Wagner, H. 1998, [A&A](#), **333**, 1
- Kerscher, M., Schmalzing, J., Retzlaff, J., et al. 1997, [MNRAS](#), **284**, 73
- Kerscher, M., Mecke, K., Schuecker, P., et al. 2001b, [A&A](#), **377**, 1
- Kitaura, F.-S., Rodríguez-Torres, S., Chuang, C.-H., et al. 2016, [MNRAS](#), **456**, 4156
- Lupton, R., Gunn, J. E., Ivezić, Z., Knapp, G. R., & Kent, S. 2001, in *Astronomical Society of the Pacific Conference Series*, Vol. 238, *Astronomical Data Analysis Software and Systems X*, ed. F. R. Harnden, Jr., F. A. Primini, & H. E. Payne, 269
- Mecke, K. R., Buchert, T., & Wagner, H. 1994, [A&A](#), **288**, 697
- Nakagami, T., Matsubara, T., Schmalzing, J., & Jing, Y. 2004, *ArXiv Astrophysics e-prints*, [astro-ph/0408428](#)
- Padmanabhan, N., Schlegel, D. J., Finkbeiner, D. P., et al. 2008, [ApJ](#), **674**, 1217
- Petri, A., Haiman, Z., Hui, L., May, M., & Kratochvil, J. M. 2013, [PhRvD](#), **88**, 123002
- Pier, J. R., Munn, J. A., Hindsley, R. B., et al. 2003, [AJ](#), **125**, 1559
- Planck Collaboration, Ade, P. A. R., Aghanim, N., et al. 2014a, [A&A](#), **571**, A23
- . 2014b, [A&A](#), **571**, A25
- . 2016, [A&A](#), **594**, A16
- Platzöder, M., & Buchert, T. 1996, in *Astro-Particle Physics*, ed. A. Weiss, G. Raffelt, W. Hillebrandt, F. von Feilitzsch, & T. Buchert, 251
- Reid, B., Ho, S., Padmanabhan, N., et al. 2016, [MNRAS](#), **455**, 1553
- Sahni, V., Sathyaprakash, B. S., & Shandarin, S. F. 1998, [ApJL](#), **495**, L5
- Sathyaprakash, B. S., Sahni, V., & Shandarin, S. 1998, [ApJ](#), **508**, 551
- Schmalzing, J. 1999, in *Evolution of Large Scale Structure : From Recombination to Garching*, ed. A. J. Banday, R. K. Sheth, & L. N. da Costa, 127
- Schmalzing, J., & Buchert, T. 1997, [ApJL](#), **482**, L1
- Schmalzing, J., Buchert, T., Melott, A. L., et al. 1999, [ApJ](#), **526**, 568
- Schmalzing, J., Kerscher, M., & Buchert, T. 1996, in *Dark Matter in the Universe*, ed. S. Bonometto, J. R. Primack, & A. Provenzale, 281
- Slepian, Z., & Eisenstein, D. J. 2015, [MNRAS](#), **448**, 9

- Slepian, Z., Eisenstein, D. J., Brownstein, J. R., et al. 2017, [MNRAS](#), **469**, 1738
- Smee, S. A., Gunn, J. E., Uomoto, A., et al. 2013, [AJ](#), **146**, 32
- Smith, J. A., Tucker, D. L., Kent, S., et al. 2002, [AJ](#), **123**, 2121
- Wiegand, A., Buchert, T., & Ostermann, M. 2014, [MNRAS](#), **443**, 241
- Wiegand, A., & Eisenstein, D. J. 2017, [MNRAS](#), **467**, 3361
- York, D. G., Adelman, J., Anderson, Jr., J. E., et al. 2000, [AJ](#), **120**, 1579
- Yoshiura, S., Shimabukuro, H., Takahashi, K., & Matsubara, T. 2017, [MNRAS](#), **465**, 394